CHAPTER-3

Zinc-Tryptophan Nanoassemblies for Antibacterial and Wound Healing Applications

3.1 Introduction:

One of the ongoing clinical issues in healthcare is wound management, which can result in serious infections and raise morbidity and death rates.[1] Microorganisms can readily infiltrate beneath the surface of injured human skin, leading to the development of wound infections. Antimicrobial-resistant pathogen exposure is also anticipated to worsen the severity and mortality of wounds. According to a study, 75% of post-operative mortality are already attributable to wound infections. The increasing prevalence of antibiotic resistance (AMR) makes treating wound infections more challenging. *Staphylococcus aureus, Escherichia coli and Pseudomonas aeruginosa* are the most often isolated bacteria from infected wounds where, these have exceptionally high rates of single- or multi-drug resistance.[2] While 88.2% of isolates had at least one antibiotic resistance, only 29.2% of isolates had multi-drug resistance to at least six antimicrobials.[3] According to numerous evaluations of *Bacillus* infections, the majority of *Bacillus* organisms were found in people who had suffered serious burns, blunt or sharp injuries, or were immunocompromised. People with wounds other than burns experienced local inflammation and minor infections due to the *Bacillus* bacterium. They may cause nosocomial bacteraemia and have the ability to create biofilms.[4] Some of these isolates were resistant to multiple drugs and displayed unique resistance patterns. Many nanomaterials (NPs) have been created, discovered, and investigated in recent years for use in antibacterial and wound-healing applications.[5,6]

Recently, zinc nanoparticles (ZnNPs) have shown promise in various biomedical applications including angiogenesis, anticancer, antibacterial, anti-inflammatory, and anti-diabetic properties.[7] It functions as a crucial cofactor for a plethora of metalloenzymes essential for cell membrane repair, proliferation, and immune function, which are critical during the wound-healing phases of coagulation, inflammation, and tissue regeneration.[8] Moreover, zinc (Zn) displays anti-inflammatory and antioxidative properties, aiding in the mitigation of oxidative stress and inflammation at the wound site.[9] Despite these advantageous effects, constraints such as bioavailability, limited stability, inadequate dispersion, insufficient interfacial interaction, and poor skin absorption and delivery of Zn to wound sites may potentially hamper its therapeutic efficiency in clinical applications.[10]

Moreover, when a possibly detrimental stimuli interrupts homeostasis it induces physiological stress and prolonged inflammatory response that results in the development of chronic stress impeding the healing of cutaneous wounds.[11] This, in turn increases the risk of infection, and mobility in patients. By decreasing the synthesis of nuclear

factor kappa-light-chain enhancer and raising the production of interleukin-10, L-tryptophan (W) therapy have shown immune regulations and anti-inflammatory effects.[12] Hence, utilization of the anti-inflammatory properties of W could help in reducing chronic stress and promoting rapid healing of cutaneous wounds. Additionally, it acts as a precursor to serotonin and other bioactive molecules that govern cellular proliferation, differentiation, and immune response.[13] W also plays a role in the synthesis of proteins necessary for tissue repair.[14] Despite several obvious advantages, the direct application of W in wound healing encounters limitations due to its poor stability and swift degradation in biological environments. It has been shown in literature that tryptophan is very important for bacterial metabolism and *E. coli* has a unique tendency to capture local tryptophan from the host for their survival.[15] Hence, tryptophan can be directly or indirectly utilized for targeting of bacteria and developing new class of antibiotics.[16] To address these limitations, herein we synthesized Zn-W complex nanosheet assemblies (Zn-W) that could substantially enhance wound healing outcomes and mitigate bacterial infections. The Zn-W nanoassemblies are designed to leverage the advantages of zinc (Zn) and tryptophan (W) while overcoming their limitations. Their biocompatibility, achieved through the incorporation of amino acid W with bioavailable Zn, ensures safe and effective applications in wound healing and biomedical contexts. The use of bioavailable Zn enhances the structural integrity, safety, and functionality of the nanosheets in biological environments. Moreover, both Zn and W are abundant and cost-effective, supporting scalable production and broad accessibility, particularly for healthcare applications requiring economical yet effective wound care solutions. The two-dimensional (2D) nanosheet morphology provides an extensive surface area, optimizing interactions with wound tissues and fostering accelerated tissue regeneration. This combination of biocompatibility, cost-efficiency, and structural advantages positions Zn-W nanoassemblies as a promising innovation in advanced wound care technologies.

3.2 Results and Discussion

3.2.1 Synthesis and Characterizations of Zn-W:

Zinc-Tryptophan nano assemblies were synthesized using a simple approach. The introduction of $ZnCl_2$ into a basic aqueous solution containing W initiates a series of noteworthy chemical and physical transformations, commencing with the conversion of the transparent mixture into a coagulated colloidal state and culminating in the formation of microcrystals **(Figure 1**).

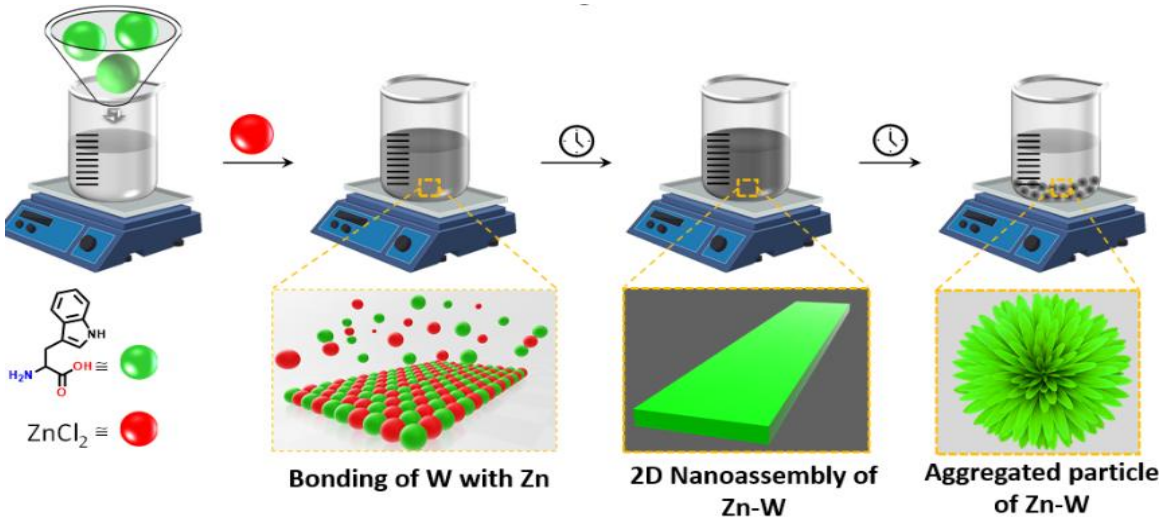

Figure 1: Schematic diagram for the steps of synthesis of Zinc-Tryptophan nanoassemblies.

This transformation is not only visually noticeable but also significantly characterized in the ultraviolet-visible (UV-vis) absorption spectra of the reaction mixture between $ZnCl_2$ and W **(Figure 2a)**. The spectra reveal extensive absorbance within the 300 to 800 nm range in the visible spectrum, indicative of the formation of colloidal nanoassemblies named Zn-W. To further explore the stoichiometric aspects of Zn-W complex formation, we utilize a Job plot **(Figure 2b)**. By measuring absorbance at a peak wavelength (λ_{max}) of 340 nm, while maintaining a constant total concentration [Zn+W] of 10 mM and varying the fraction of Zn(II) ions, an inflection point is discerned at a Zn (II) fraction of 0.3. This observation emphasizes a 1:2 binding stoichiometry between Zn (II) ions and W, providing clarity on the interaction mechanisms.

The subsequent analytical investigation, using Electrospray Ionization Mass Spectrometry (ESI-MS), has significantly supported the preliminary findings by identifying a mass peak at m/z = 505.5 **(Figure 2c, Figure 3 is the Full mass spectra correspond to Figure 2c)**.

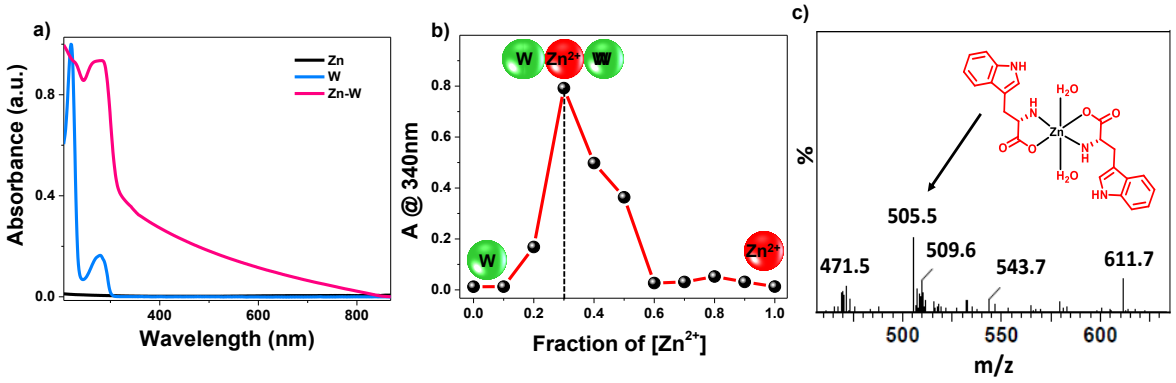

Figure 2. (a) UV-visible absorption spectra of W and Zn-W. **(b)** Complexation job plot constructed by plotting absorbance at 340nm against the fraction of Zinc ions (Zn2+) concentration. **(c) Selected area ESI** mass spectrometric analysis of Zn-W; inset showing the chemical structure of Zn-W.

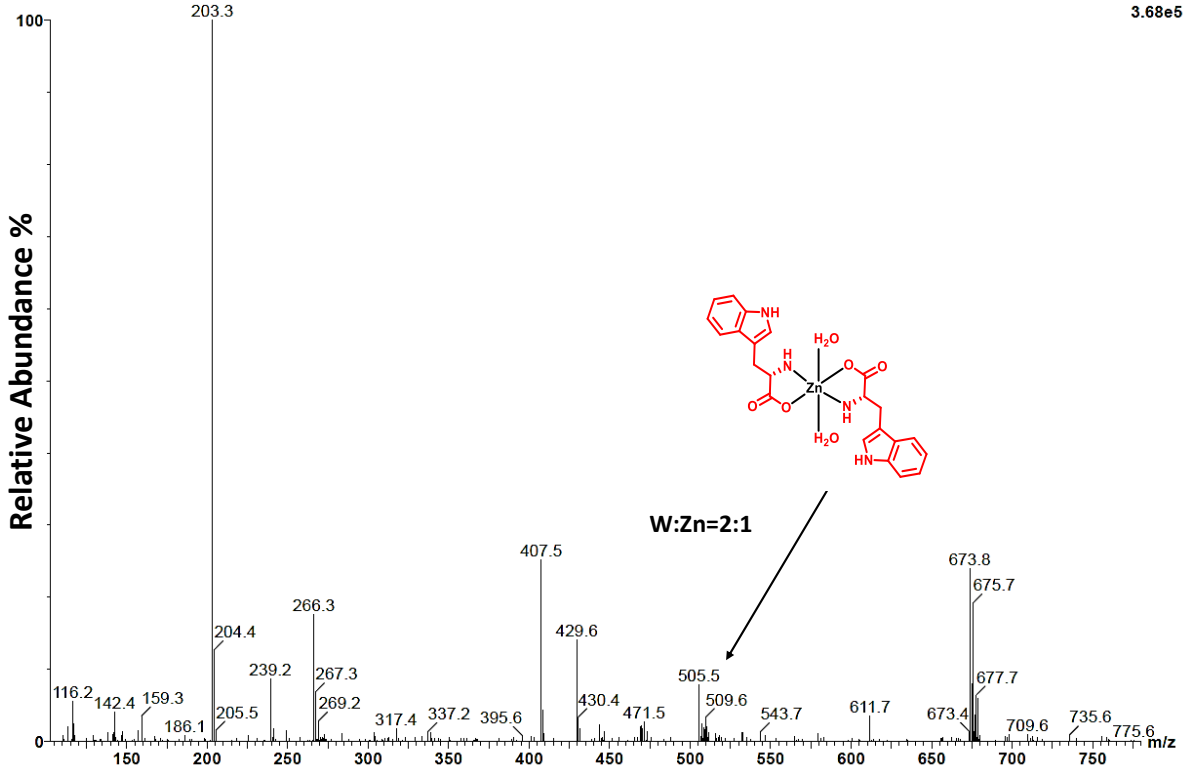

Figure 3. Full mass spectra correspond to the figures 2c.

This observation aligns with the predicted molecular mass of the $[Zn+W_2]$ $(H_2O)_2$ complex, thereby reinforcing the hypothesized 1:2 stoichiometric ratio between Zn (II) and W. The Fourier Transform Infrared (FTIR) spectra analysis comparing free W with the Zn-W assembly has provided valuable insights into the coordinating behavior of Zn-W **(Selected area FT-IR spectra Figure 4a, Figure b, Full FT-IR spectra correspond to Figure 4a)**. It is evident from the absence of a peak at 3014 cm^{-1} in the Zn-W assembly spectrum, which is characteristic of the $-NH_3^+$ stretching vibrations found in free W, that the $-NH_3^+$ group in W has engaged in

coordination with the Zn (II) ion, transitioning to its deprotonated form.[17] Further analysis of the carboxylate (-COO^-) group of free W reveals asymmetric and symmetric stretching peaks at 1660 cm^{-1} and 1580 cm^{-1}, respectively, with a peak splitting value of $\Delta\upsilon = 80$ cm^{-1}. However, in the Zn-W assembly, these signals undergo a significant energy shift, with the asymmetric stretching peak at 1620 cm^{-1} and the symmetric stretching peak at 1595 cm^{-1}, resulting in a decreased peak splitting value of $\Delta\upsilon = 25$ cm^{-1}, indicating a chelating mode of binding with Zn (II). Additionally, the absence of the peak at 624 cm^{-1}, corresponding to the in-plane bending vibration of the -COO^- group in the Zn-W assembly, denotes the formation of a COO-Zn bond.[18,19] These spectral findings firmly establish the coordination between W and Zn (II) through both its amine (-NH_2) and carboxylate (-COO^-) groups, leading to the formation of a chelate configuration **(Figure. 2C inset)**. This provides a comprehensive understanding of the intricate interaction dynamics within the Zn-W assembly, shedding light on the molecular underpinnings that facilitate such coordination.

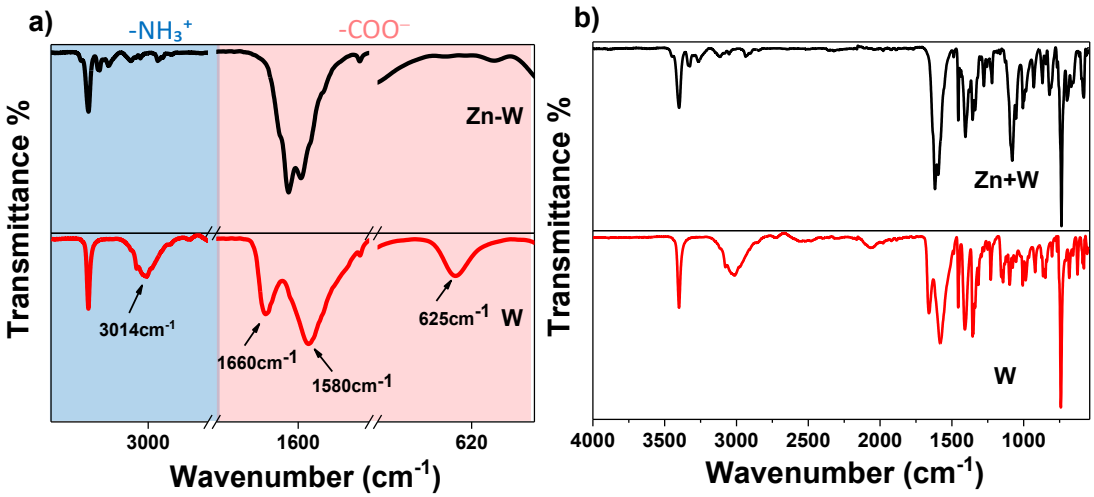

Figure 4. (a) Selected area FT-IR spectra of W and Zn-W. **(b)** Full FT-IR spectra of W and Zn-W material.

Next, the intricate assembly structures were examined High-Resolution Scanning Electron Microscopy (HR-SEM). The examination uncovered the development of micro-scale spherical particles and elaborately detailed flower-like structures made of 2D microcrystals **(Figure 5a, b)**. Energy Dispersive X-ray (EDX) spectroscopy verified the elemental composition, highlighting the presence of zinc (Zn), carbon (C), nitrogen (N), and oxygen (O) within the produced Zn-W 2D microcrystals with their respective percentages **(Figure 5c)**. Further studies using High-Resolution Transmission Electron Microscopy (HR-TEM) revealed the presence of precise rectangular 2D nanosheets **(Figure 6a)**. The Selected Area Electron Diffraction (SAED) patterns from these nanosheets unambiguously confirmed their crystalline nature **(Figure 6b)**. Additionally, the Powder X-ray Diffraction (PXRD) patterns not only revealed a

distinct diffraction pattern from that of W alone but also validated the crystalline structure of the Zn-W complexes **(Figure 7)**. Dynamic light scattering studies demonstrated a hydrodynamic diameter range of ~1000-1400 nm for the Zn-W nano assemblies in phosphate buffer saline (PBS) solution. The size of the Zn-W did not change significantly at day 11 in PBS (~1450-1950 nm), indicating good colloidal stability.

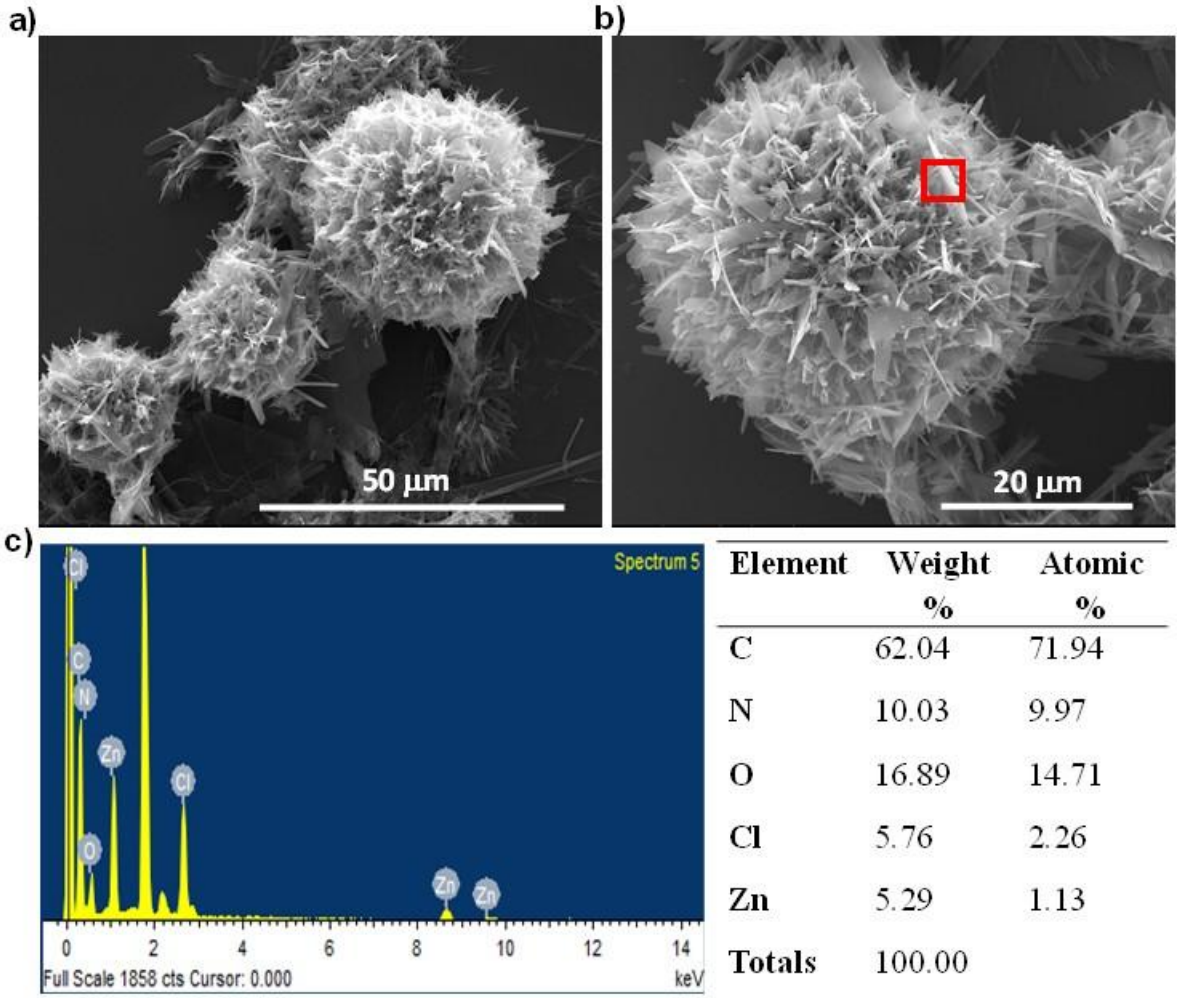

Element	Weight %	Atomic %
C	62.04	71.94
N	10.03	9.97
O	16.89	14.71
Cl	5.76	2.26
Zn	5.29	1.13
Totals	100.00	

Figure 5. (a-b) High-resolution scanning electron microscope (HR-SEM) image of Zn-W (a) at scale bar 50 µm; b) at scale bar 20 µm). **(c)** Energy-dispersive X-ray spectroscopy (EDS) spectra of Zn-W structure recorded at the red box area in **(b)**.

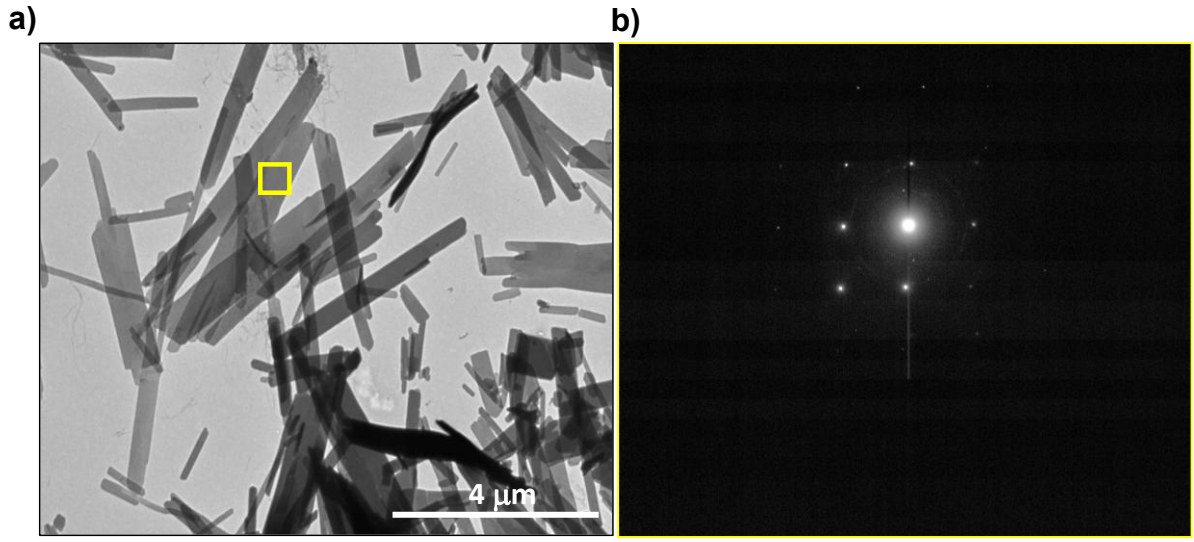

Figure 6. (a) High-resolution transmission electron microscope (HR-TEM) images of Zn-W (scale bar 1 mM). **(b)** Selected area electron diffraction (SAED) pattern of Zn-W nanostructure recorded at the yellow box area in Figure **(a).**

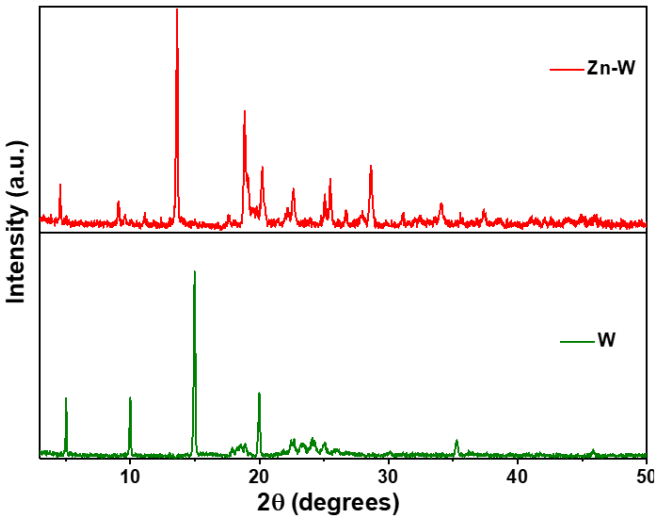

Figure 7. Comparison of Powder X-ray diffraction (PXRD) patterns of W and Zn-W.

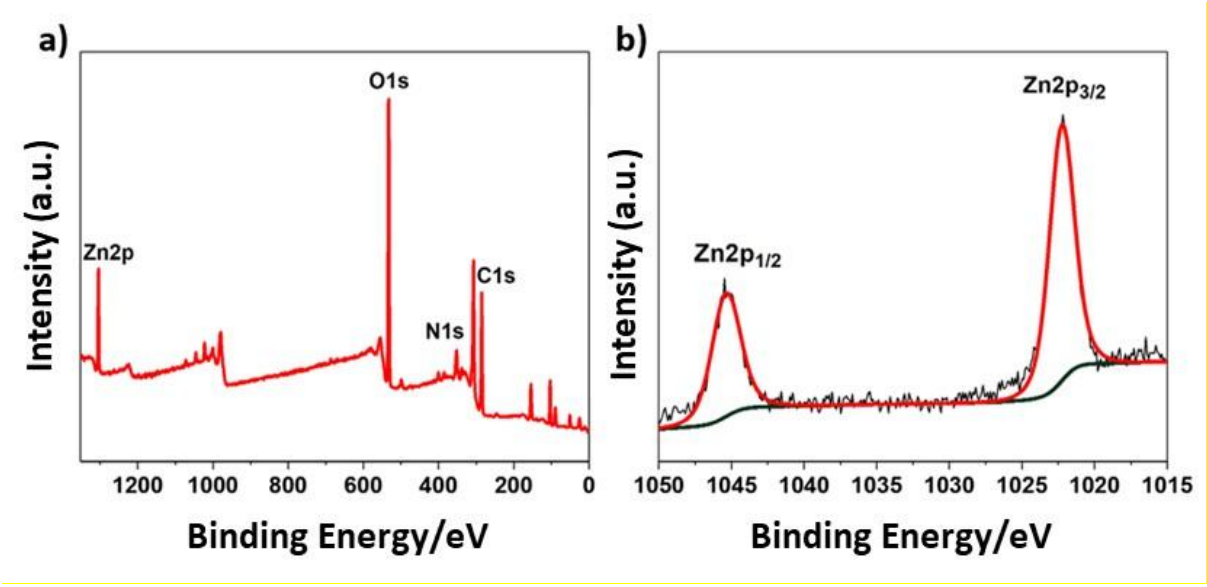

Figure 8: **(a)** XPS Survey spectra indicate the presence of zinc (Zn) along with carbon (C), nitrogen (N), and oxygen (O), highlighting their respective chemical states. **(b)** The Zn2p scan spectra reveal distinct peaks corresponding to Zn2p3/2 and Zn2p1/2.

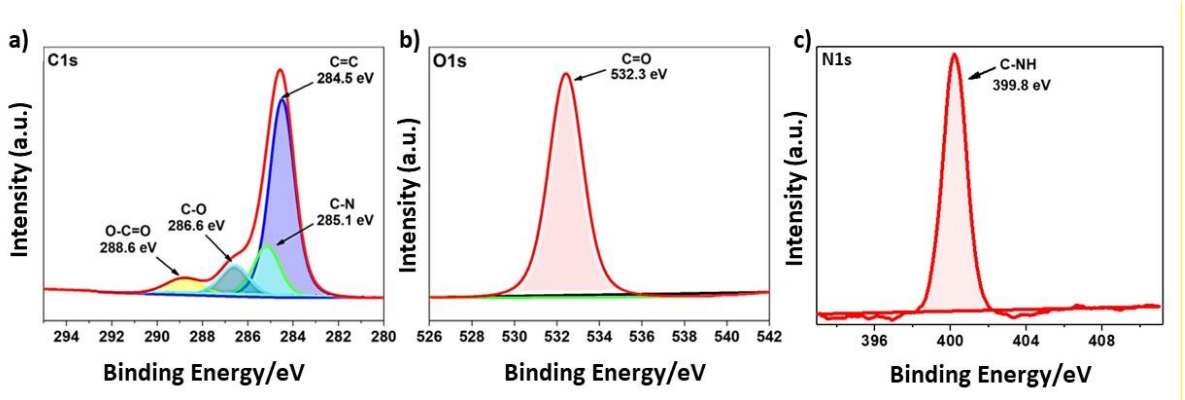

Figure 9. (a) The C1s fitted spectra illustrate the peaks associated with the primary functional groups present in the Zn-W assemblies. **(b)** The O1s spectra exhibit a single peak corresponding to the carbonyl functional group. **(c)** The N1s spectra exhibit a single peak corresponding to the carbon-NH functional group.

The X-ray Photoelectron Spectroscopy (XPS) analysis was conducted to facilitate a comprehensive characterization of the Zn-W nanomaterial, as delineated in Figure 2. The collective XPS survey spectrum confirmed the presence of zinc (Zn), oxygen (O), nitrogen (N), and carbon (C) elements, with characteristic peaks identified at binding energies of 1022.2 eV, 532.4 eV, 400.3 eV, and 285 eV, respectively **(Figure 8a)**. High-resolution XPS spectra further elucidated the electronic states, revealing peaks at 1022.1 eV and 1045.3 eV, which are associated with the Zn^{2+} states of Zn 2p3/2 and Zn 2p1/2, respectively **(Figure 8b)**. Additionally, a detailed deconvolution of the C1s region identified peaks at binding energies of 284.5 eV, 285.1 eV, 286.6 eV, and 288.6 eV, corresponding to various functional groups, specifically C=C, C–N, C–O, and O–C=O **(Figure 9a)**. Moreover, **Figures 9b** and **9c**

illustrated the presence of C=O and C–NH functional groups within the Zn-W assemblies, with binding energies recorded at 532.3 eV and 399.8 eV respectively. These findings substantiate the functionalization and chemical composition of the Zn-W nanomaterial, thereby reinforcing its structural integrity.

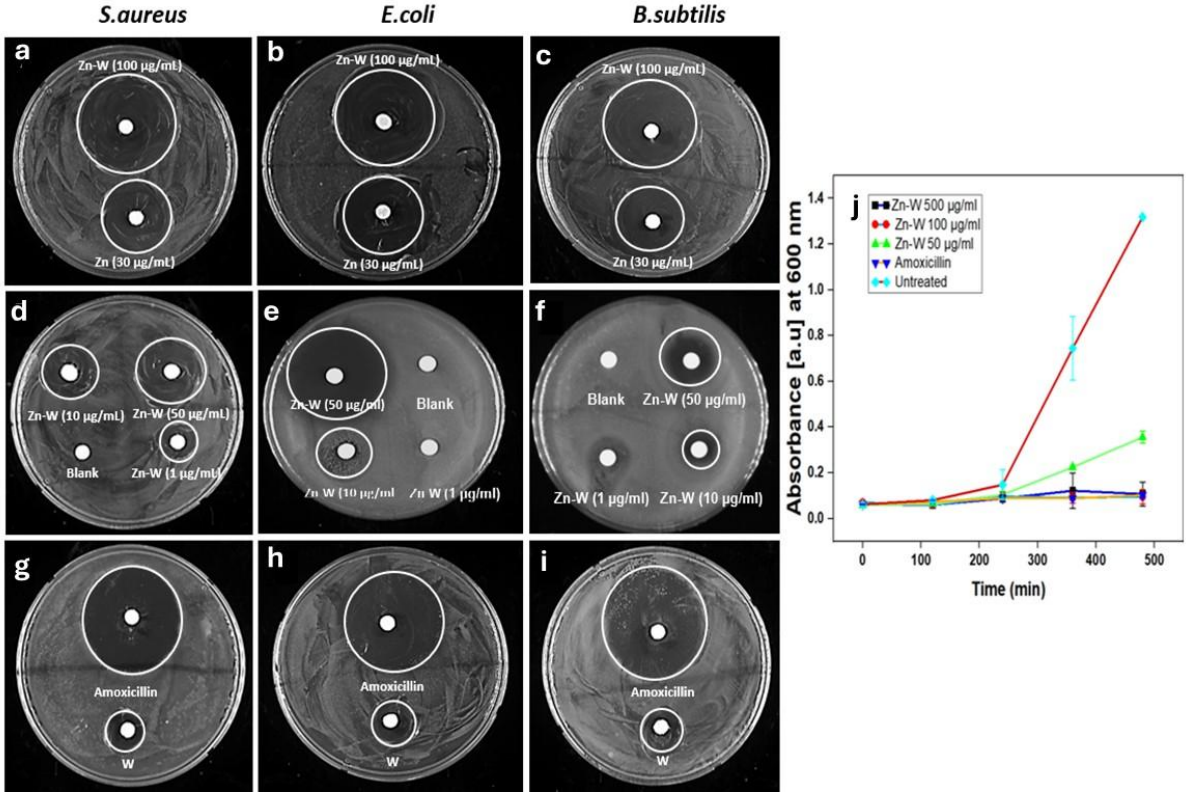

Figure 10. (a, d, g) Gel Doc images of the *S. aureus*. **(b, e, h)** images of *E. coli* and **(c, f, i)** images of *B. subtilis* with varying concentrations of Zn-W (100, 50, 10, and 1 µg/ml) and only Zinc 30 µg/ml and tryptophan 70 µg/ml treatment in comparison to the untreated control group for zone of inhibition study. **(j)** The growth inhibition curve of *E. coli* in the presence of various Zn-W concentrations (500 100 and 50 µg/ml), positive control amoxicillin (0.684 mol/L) and untreated control (n=3 for all groups). Statistical analysis was done using one-way ANOVA followed by the Tukey test, where $p < 0.05$.

3.2.2 Antimicrobial activity of Zn-W:

The ability of wound dressings to withstand bacterial adhesion is essential for reducing the development of biofilm and averting wound infections. Zone of inhibition (**Figure 10a-i)** showed that treatment with various Zn-W concentrations (100, 50, 10, and 1 µg/ml) and also with Zn and W respectively. The treatments reduced the growth of both gram-negative (*E. coli*) and gram-positive (*B. subtilis and S. aureus*) bacterial colonies. Whatman filter paper has been used in our study of antimicrobial assays, due to its consistent quality, uniform porosity. The cellulose-based structure of Whatman paper ensures compatibility with aqueous solutions, allowing nanoparticles to diffuse efficiently into the agar medium without significant

interference.[20] The outcomes showed that, at concentrations of 100 and 50 μg/ml, Zn-W is more effective at killing *E. coli*, *S. aureus* and *B. subtilis*. Moreover, the BGI (Bacterial Growth Inhibition) test findings verified that Zn-W exhibits dose-dependent bacterial growth inhibition in *E. coli.* **(Figure 10j)**.

3.2.3 SEM examination showed that Zn-W disrupts *E. coli* biofilms:

SEM analysis was done to determine the extent of damage to the biofilms formed by *E. coli* bacterial strains in presence of Zn-W. The SEM images **(Figure 11 c-d)** showed that the biofilm treated with Zn-W lost its architecture and structural integrity. In contrast, the *E. coli* bacteria that were left untreated produced a mature film while retaining their structural integrity **(Figure 11 a-b)**. Moreover, the number of bacteria in the Zn-W treated group has significantly reduced compared to the untreated control group. This finding suggests that Zn-W damages the bacterial wall and structural proteins, resulting in the killing of the bacteria and impairing the integrity of the biofilm. After exposure to Zn-W for 6-8 hr, bacterial cells were stained with DCFH-DA for 30 min. It was observed that the Zn-W treated bacteria became DCF^{+}, whereby the green fluorescent cells indicate that ROS were generated and participated in the nanoparticle mediated cell death **Figure 11e**.

3.2.4 Intracellular Production of reactive oxygen species (ROS) by Zn-W:

The bandgap of zinc is 3.3 eV, making it a direct semiconductor. Therefore, when exposed to UV radiation, all of its valence and conduction bands have the ability to produce electron-hole pairs. Hydrogen peroxide (H_2O_2), superoxide anion (O^{2-}), and hydroxyl radicals ($OH\cdot$) are examples of ROS that are produced when water and oxygen molecules come in contact to the surface of the Zn-W. ROS produced by the Zn-W may causes oxidative damage that ultimately results intracellular death. To confirm the intracellular ROS generation by the treatment of Zn-W (500, 100, 50, and 10 μg/ml), DCFDA assay was performed. Amoxicillin with a concentration of 1000 μg/ml was used as a positive control. **Figure 11f** showed that Zn-W produced dose dependent ROS confirmed by the presence of green fluorescence that is higher compared to the untreated control group and positive control.

3.2.5 Impact of Zn-W in the bacterium's extracellular polymeric substances (EPS):

Biofilms are formed when bacteria adhere to surfaces and produce extracellular polymeric substances (EPS). Increased EPS production will change the architecture of biofilms, making them more resistant to antibacterial agents. In order to assess the impact of chemically produced Zn-W nano assemblies on the formation of extracellular polysaccharides in bacterial isolates, the dry weight of the extracted EPS was determined following the treatment. The findings

demonstrated a decrease in the EPS when treated with Zn-W (100 and 50 µg/ml) as compared to untreated cells **(Figure 11g)**.

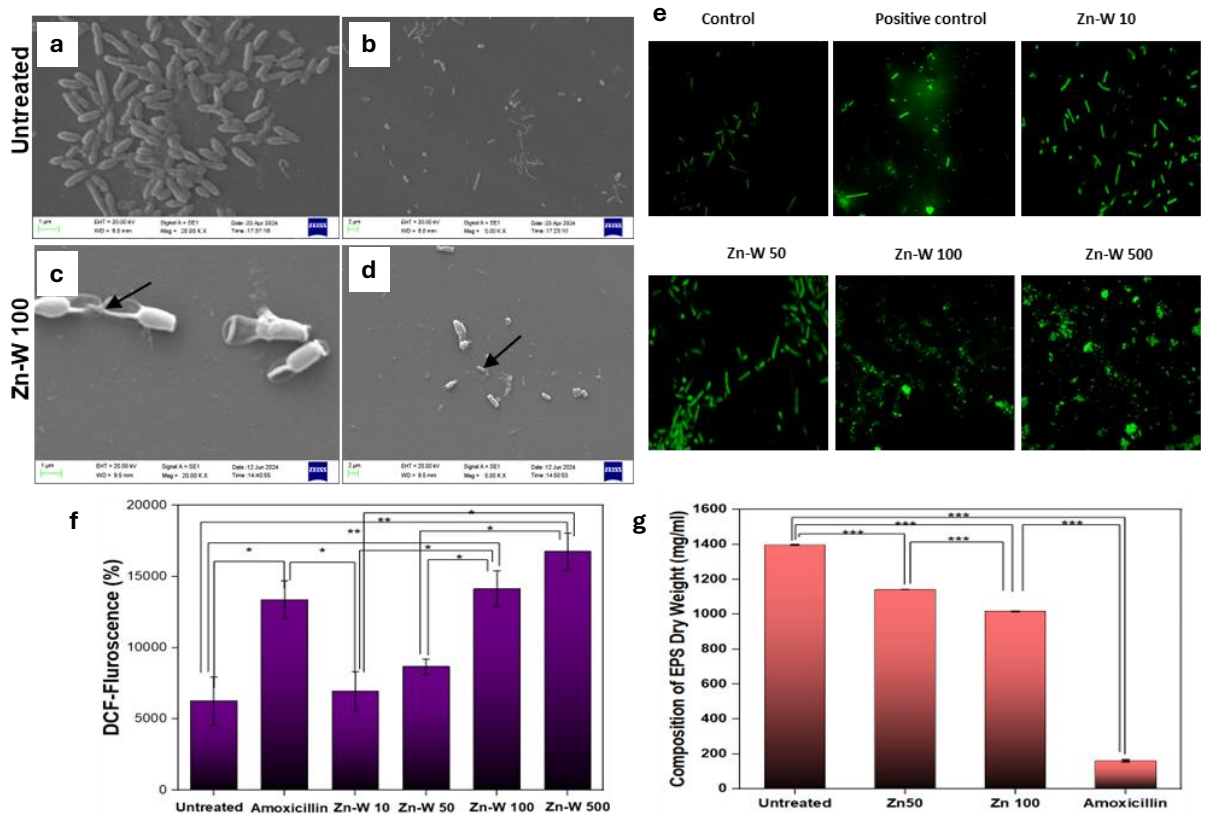

Figure 11. (a, b) SEM images of E. coli taken without treatment in different magnifications (20× and 5×). **(c, d)** SEM pictures of E. coli in the presence of Zn−W coated coverslips. The breaking and shattering of the bacterium membrane is indicated by the black arrows. **(e)** Confocal images showing intracellular ROS generation inside bacterial cell. **(f)** Intracellular ROS production in E. coli by the treatment of various doses of Zn−W (500, 100, 50, and 10 µg/mL). Amoxicillin antibiotic (1000 µg/mL) is used as a positive control ($p < 0.001$). **(g)** Impact of Zn−W in the bacterium's EPS. Statistical analysis ($n = 3$) was done using one-way ANOVA followed by the Tukey test, where $p < 0.05$

3.2.6 Confocal microscopy for biofilm inhibition by Zn-W:

Confocal microscopy facilitates the visual monitoring of the biofilm's elimination following Zn-W treatment at different concentrations. *DAPI* and *PI* staining were used to evaluate the total bacterial (GFP-tagged *E. coli*) population of live and dead cells in each group. Blue *(DAPI)* fluorescence shows the total bacterial cells (live + dead) **(Figure 12a-c). Figure 12** demonstrated that the untreated control group had more adherent bacterial cells and living biofilm (more green and blue cells). Conversely, the Zn-W treatment at different concentrations (100 and 500 µg/ml) resulted in a large increase in the number of dead bacteria (greater red fluorescence) and a significant decrease in the attachment of live bacteria (indicated by the lower amount of green and blue fluorescence). Additionally, the fluorescence intensities for

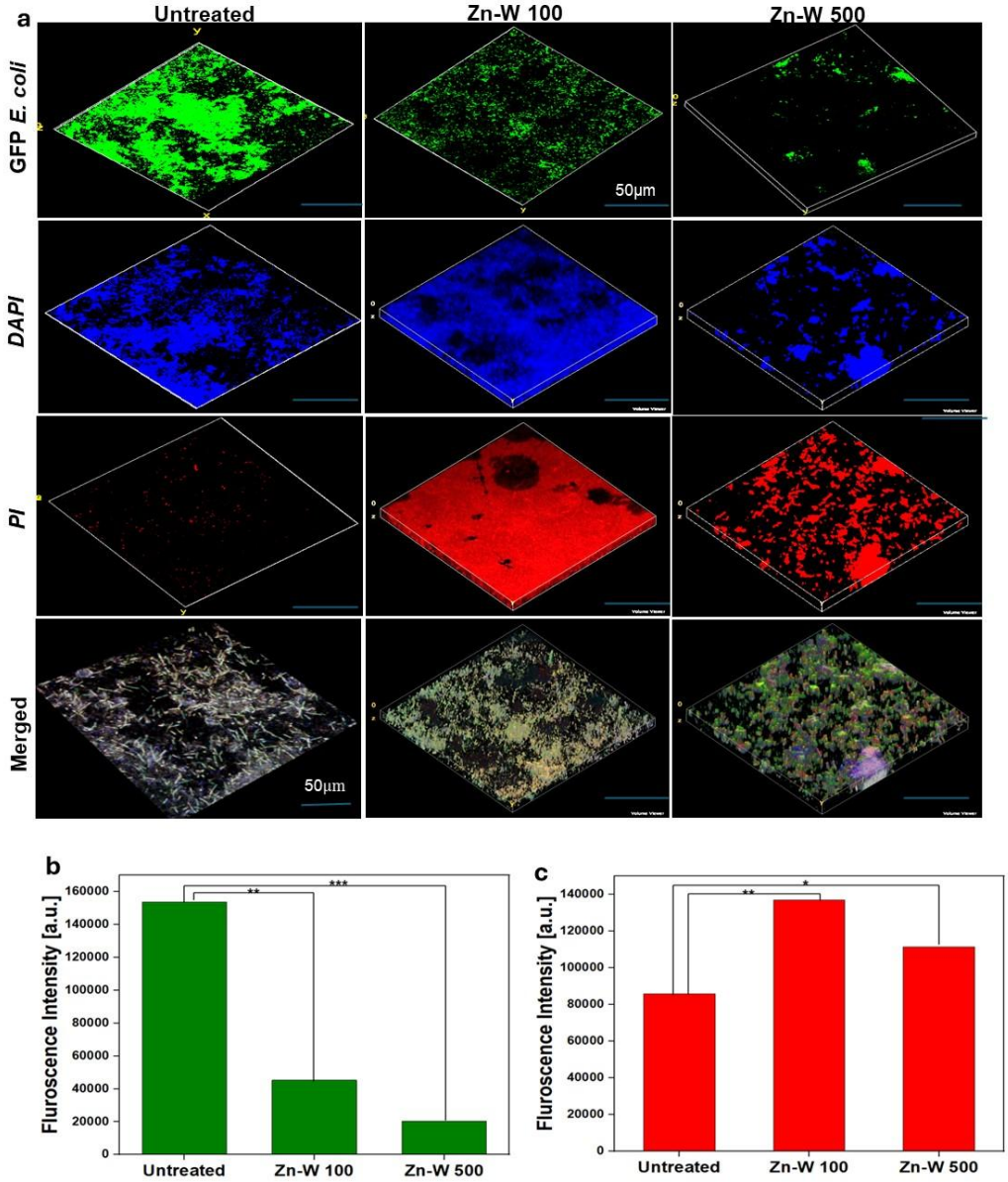

Figure 12. Different concentrations of Zn-W-treated (concentration 100 and 500 µg/ml) and untreated 3D confocal pictures of E. coli. **(a) GFP-*E. coli* Panel**: The green fluorescence indicates that living bacteria have attached; ***DAPI* Panel**: Blue fluorescence revealed by *DAPI* staining indicates the total number of adherent bacteria; ***PI* Panel**: The red fluorescence produced by the *PI* staining indicates the number of dead bacteria; **Merged Panel**: Fluorescence Confocal Merged Images. **(b-c)** The green and red fluorescence quantification plot of all live and dead *E. coli* adhering to coated Zn-W compared to untreated. Statistical analysis was done using one-way ANOVA followed by the Tukey test, where $p < 0.05$.

each group were quantified using Image J software, and the results are shown in **(Figure 12b-c)**. The green fluorescence intensity was found to be higher in the untreated than in the Zn-W treated group, indicating a considerable reduction in biofilm after treatment (**Figure 12b**). **Figure 12c** verifies that there are more dead bacteria in the Zn-W group than untreated group.

These results clearly imply that Zn-W has potent antibiofilm properties that negatively impact the adhesion and development of bacteria.[21] The findings of the studies indicated that Zn-W has both antibacterial and antibiofilm properties.

3.2.7 Zn-W showed biocompatibility in chicken embryonic model:

The chorioallantoic membrane assay (CAM) assesses changes in blood vessel growth and connections to ascertain a material's suitability for use in living tissue. Blood vessel images of chick embryos were captured using a stereo microscope at different times, up to six hours after treatments were administered. The results displayed in **(Figure 13 a-f)** demonstrate that Zn-W treatments did not impair the development of blood vessels or the vascular architecture in chick embryos up to 100 µg/ml dose. Several metrics related to blood vessels integrity were evaluated, including size, length, and junctions were quantified and showed no significant changes following Zn-W treatment, indicating biocompatibility **(Figure 13 g-i)**.

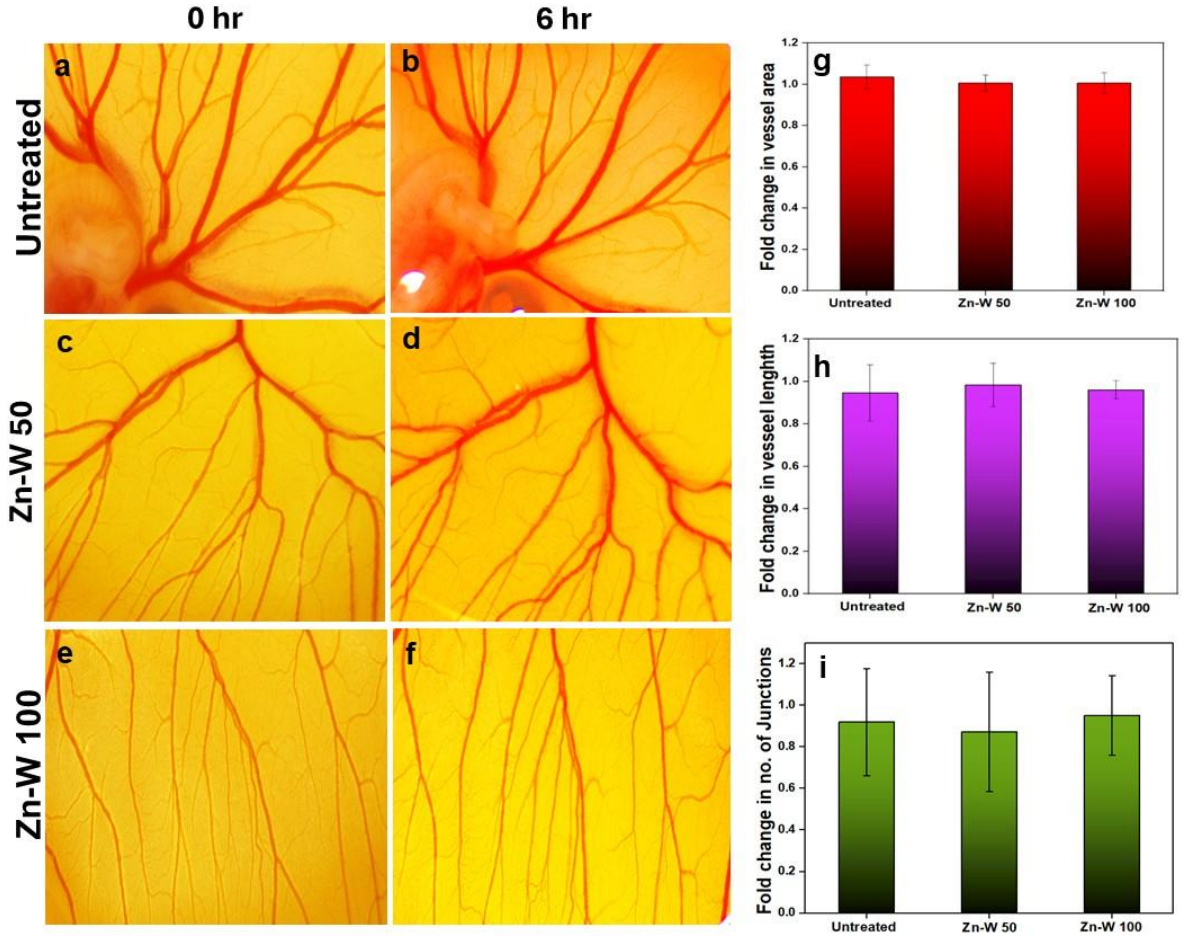

Figure 13. (a-f) The stereo microscopic pictures of the untreated and Zn-W treated chick embryo models (concentration 100 and 50 µg/ml) at 0 and 6 hours are displayed in (n=3). **(g-i)** The images are quantified in terms of length, junction, and size using tools such as ImageJ and Angiotool. test results are displayed as mean±SD (*p>0.05).

3.2.8 Zn-W are non-toxic to human cell line and promotes cell proliferation:

MTT assay was used to evaluate the cytotoxicity of Zn-W in HEK-293 (human embryonic kidney) cells. Results show the cytocompatibility of Zn-W across different doses (10–100 μg/ml) for 24 hours. Hence, Zn-W can be successfully utilized for different biomedical applications at their therapeutic dose (100 μg/ml) **Figure 14f.** We conducted cell proliferation assays using the 5-ethynyl-2'-deoxyuridine (EdU) method to evaluate the effects Zn-W on cell proliferation in HEK-293 cell lines for 24 hours. Our results demonstrated that Zn-W at doses of 50 μg/mL and 100 μg/mL significantly promoted cell proliferation, as evidenced by the increased incorporation of EdU into the DNA of treated cells compared to untreated control as shown in **(Figure 14c).**

3.2.9 Scratch wound assay

The migration of (human embryonic kidney) cells lines was determined using a scratch assay, the effects of different concentrations of Zn-W on cell migration were investigated and it was found that Zn-W promoted cell migration within a concentration range (50-100 μg/mL) in a dose and time dependent manner **Figure 14a**. A wound closure plot showing Zn-W 100, promoting cell migration followed by Zn-W 50 with respect to control **Figure 14b.**

3.2.10 Measurement of cellular internalized ROS

In our study, we assessed the impact of zinc-tryptophan nanoassemblies on reactive oxygen species (ROS) production in HEK 293 cells. The results indicated a concentration-dependent effect on ROS levels, as measured by fluorescence intensity. At a concentration of 500 μg/ml, the nanoassemblies produced the least fluorescence, indicating lower ROS production. This was followed by 100 μg/ml, 50 μg/ml, and 10 μg/ml, which exhibited progressively higher fluorescence intensities **Figure 14e**. These findings suggest that higher concentrations of zinc-tryptophan nanoassemblies may induce cellular mechanisms that mitigate oxidative stress.

This is in accordance with the antioxidant assay we performed using DPPH assay where a direct relationship has shown in the anti-oxidant property of the Zn-W with their dose (**Figure 14d**).

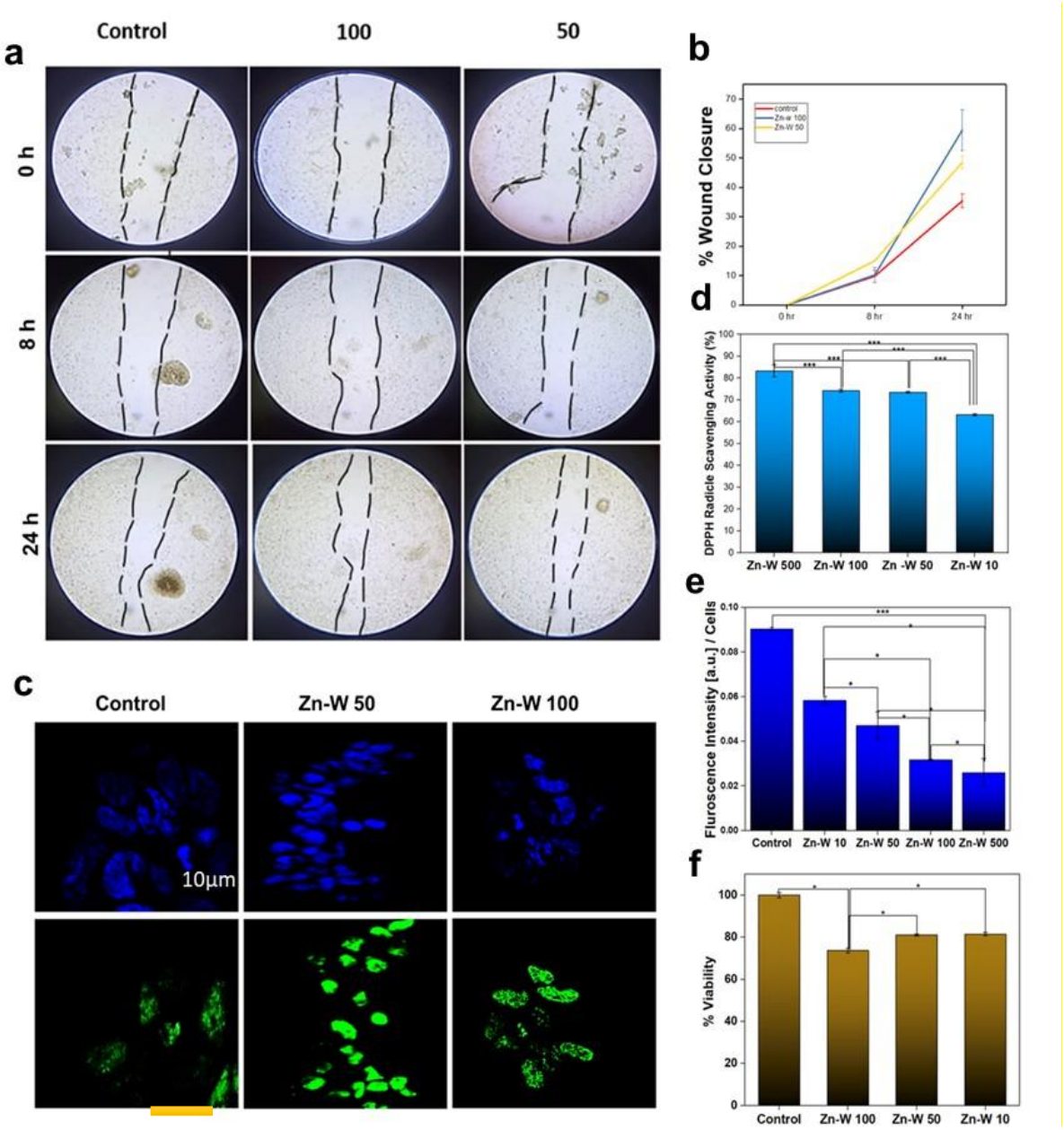

Figure 14: (a) Evaluation of wound scratch assay for 24 h in HEK-293 cell lines using bright-field microscopic images. **(b)** Wound closure plot showing Zn−W100, promoting cell migration followed by Zn−W50 with respect to control (n = 3). **(c)** Images showing cell proliferation assay in HEK-293 cell lines for 24 h of treatment with Zn−W (50 and 100 µg/mL; n = 3). **(d)** Antioxidant studies of Zn−W using the DPPH assay at different doses (500, 100, 50, and 10 µg/mL); n = 3. **(e)** Zinc−tryptophan nanoassemblies on ROS production in HEK 293 cells (n = 3). **(f)** MTT assay to evaluate the cytotoxicity of Zn−W in HEK-293 (human embryonic kidney) cells at different doses (10−100 µg/mL) for 24 h treatment (n = 3). Statistical analysis was done using one-way ANOVA, followed by the Tukey test, where $p < 0.05$.

3.3 *In vivo* wound healing mediated by Zn-W treatment:

The *in vivo* wound healing of $LiAlO_2$was assessed. Using a punch biopsy method, the wounds were created on the rat's dorsal side. On days 0, 3, 5, 7, 9 untreated, positive control (Silver Nitrate Gel 0.2% W/W) and $LiAlO_2$ (100 µl per rat were used as therapy on the wound area

(Figure 15a). At day 9, the $LiAlO_2$treated group's wounds nearly healed (~95%), but the untreated group's wound repair was only ~80% **(Figure 15b-c)**.[22] Histology and collagen staining analysis was performed to evaluate the effectiveness of Zn-W in the healing of skin wounds. The black arrow in **(Figure 15d-f)** depicts the re-epithelialization with a correct thicker epidermis layer without any break or rupture on the dermal layer of rat's skin treated with Zn-W. However, the untreated control group exhibits an inconsistent dermal structure and a damaged dermal layer. Further, the thickness of the epidermis was also measured for all the groups as depicted in (**Figure 15g).** Results showed that Zn-W treated tissue has thicker epidermis layer compared to positive control and untreated control group, indicating efficient healing of the rat wounds.

Collagen, which is a part of the extracellular matrix, is essential for wound healing. It acts as a scaffold where damage has occurred, establishing a bed for inflammatory cytokines and growth factors to initiate the healing process of wounds.[23] The Zn-W treated group showed a darker staining, indicating thicker and more uniformly distributed collagen deposition when stained with 0.5% aniline blue staining, as seen in (**Figure 15h-j)** compared to untreated group. Further, careful observation of images highlight that Zn-W treated tissues has more uniform and intact epidermis layer (indicated by black arrow) compared to the inconsistent and ruptured epidermis for the untreated control and positive control group. This further support the potent wound healing efficacy of the Zn-W in the *in vivo* rat model.

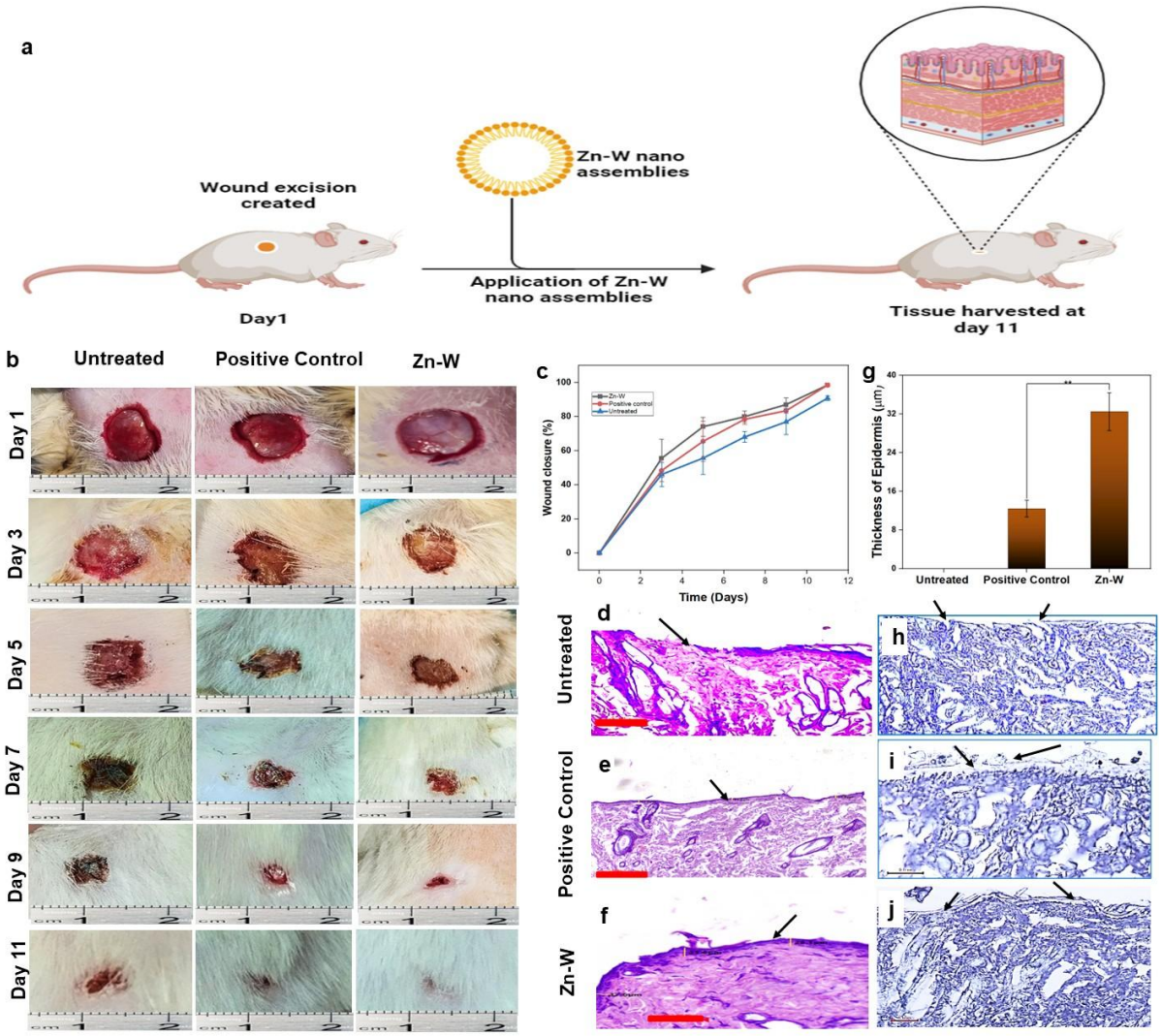

Figure 15. *In vivo* wound healing investigation of Zn-W in the rat model (n=4). **(a)** Schematic representation of application of Zn-W on Wistar rat wound model, **(b)** Optical images of the wounds for the Untreated, Positive Control (Silver Nitrate Gel 0.2% W/W) and Zn-W treated groups (20 µg per rat) from day 0 to day 11. **(c)** The time dependent percentage wound closure curve for the treated and untreated groups. **(d-f)** The H&E-stained microscopic image of the rat skin wounds for the Untreated, Positive Control and Zn-W treated groups at day 12; Pictures were taken with a 20X magnification. **(g)** Quantification of epidermis layer thickness (in 20 µm) using ImageJ analysis. **(h-j)** Microscopic images for the collagen deposition and tissue histology of various groups. Aniline blue staining was used to assess the amount of collagen deposition during granulation tissue formation. Statistical analysis was done using one-way ANOVA followed by the Tukey test, where $p < 0.05$.

Smooth muscle actin (α-SMA) immunostaining was done to stain the fibroblast cells and to understand the extent of revascularization during the wound healing process following Zn-W treatment. Higher *α-SMA* expressions in the Zn-W treated group was observed compared to the untreated group indicating greater recruitment of myofibroblast **(Figure 16a-j)**.[24] Remarkably, Zn-W aid in the process of neovascularization, or the formation of new blood vessels. The

findings support that Zn-W can heal skin wounds entirely than untreated group, while causing no harm to the local skin tissues.

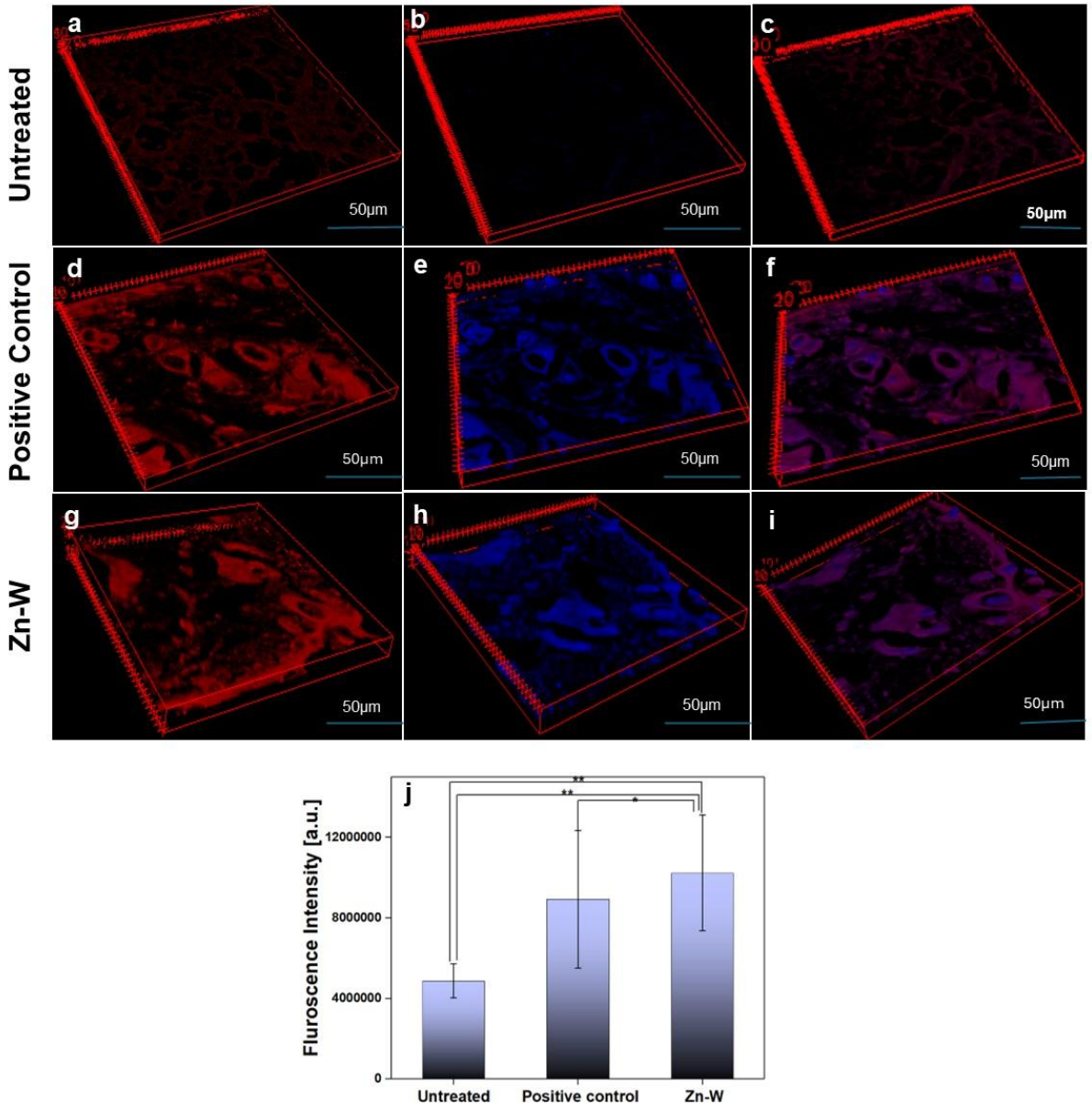

Figure 16. (a-i) 3D images showed higher $\alpha - SMA$ levels of fluorescence in the treated group Zn-W compared to the untreated group indicating more recruitment of myofibroblast. **(j)** Plot of fluorescence intensity.

3.4 Proposed Mechanism:

Zinc turns out to be a complex player in naturally during wound repair. At the site of a wound, the human body releases zinc in low amounts varying from 1 to 20 parts per million. This helps to combat infection, regulate reactive oxygen species, adjust the response to inflammation, and function as a cofactor for multiple enzymes that support granulation tissue generation, encourage vascularization, and aid in wound closure.[25,26] Zinc ions release help to control

reactive oxygen species (ROS) and inflammation by regulating macrophage polarization, which leads to the early formation of granulation tissue.[27,28] By the cooperative effects of both zinc ions and tryptophan residues into a single system (Zn-W), we attempted to support and embrace the body's natural ability to heal itself, leading to the restoration of skin tissue integrity and function.

. Conversely, tryptophan inhibits the production of biofilms and enhance the antibacterial property of the Zn-W nanoassemblies. Negative bacterial membrane charge further facilitates the internalization of Zn^{2+} ions following the dissolution of Zn-W in aqueous solutions. This ultimately leads to the death of the bacterial cell by depolarizing and distorting the membrane, generating significant amount of ROS and rupturing the bacterial membrane by the sharp surface edges of Zn-W.

3.5 Conclusion

This study summarizes the efficient method for synthesizing Zn-W 2D nanostructures, along with their multifunctional biomedical applications. The findings exhibit potent antibacterial properties against both gram-negative and gram-positive bacteria, while also demonstrating an inhibitory effect on biofilm formation. The DPPH test revealed the antioxidant capability of Zn-W, shedding light on its potential mechanism for wound healing. When compared to untreated samples, Zn-W based wound treatment significantly accelerated wound healing in rat models. These findings highlight the versatile, (4-in-1) biomedical applications of Zn-W, supporting great utility for the effective treatment of skin wounds and bacterial infections.

3.6 Experimental Section:

1. Materials

L-Tryptophane, Zinc chloride anhydrous, milli water, Sodium hydroxide, All materials were used were purchased from sigma Aldrich. 2′,7′-dichlorodihydrofluorescein diacetate (DCFH-DA) were purchased from Sigma-Aldrich. LB broth and nutrient agar were purchased from HiMedia Laboratories Pvt. Ltd. 4′,6-Diamidino-2-phenylindole (DAPI), propidium iodide (PI), 2,2-diphenyl-1-picrylhydrazyl (DPPH), DMSO, PBS and glutaraldehyde were obtained from SRL (Sisco Research Laboratories Pvt. Ltd.) - India. GFP-tagged *E. coli* was a generous gift from Prof. Bama Charan Mondal, BHU, Varanasi, and *B. subtilis* was a generous gift from Prof. Avnish Parmar, IIT BHU and *S.aureus* is obtained by IMS (Institute of Medical Sciences) BHU.

2. Synthesis of Zn-W nano assemblies

L-Tryptophan (W) (10 mM) and sodium hydroxide (10 mM) were dissolved in 50 ml of double-distilled (DD) water and sonicated for 10 minutes at room temperature to ensure complete dissolution and obtain a clear alkaline W solution. Then, zinc chloride (5 mM) was added to the alkaline W solution with stirring, resulting in the formation of curdy precipitation over time. After twelve hours of stirring for crystallization, spherical microcrystalline Zn-W particles settled at the bottom of the beaker. The settled Zn-W microcrystals were filtered and washed with excess DD water and ethanol to eliminate any remaining unreacted W, NaOH, and $ZnCl_2$. Subsequently, the collected Zn-W microcrystals were dried under a vacuum and prepared for further studies. The UV-visible absorption analysis was conducted using the Agilent Cary-60 UV-visible spectrophotometer. Optical images of the Zn-W structures were captured using the Olympus C43 microscope.

3. Characterizations Techniques Used in This Study:

3.1 UV-vis Spectrophotometer: The complexation between Zn (II) and W were studied using a UV-visible spectrophotometer (An Agilent Cary-60).

3.2 High-Resolution Scanning Electron Microscopy (HR-SEM): Zn-W samples were coated with Cr after being placed on a clean microscope glass coverslip. The images were snapped with a JSM-6700 field emission scanning electron microscope (JEOL, Tokyo, Japan) with the voltage set to 10 kV.

3.3 High Resolution Transmission Electron Microscopy (HR-TEM): Tecnai G2 20 TWIN, FEI Company of USA (S.E.A.) was used to click HR-TEM pictures with varying magnification.

3.4 Fourier Transform Infrared Spectroscopy (FT-IR): The Zn-W crystals were dispersed in anhydrous methanol and drop cast onto KBr IR card (International Crystal Labs, Garfield, New Jersey, USA) followed by vacuum drying at room temperature. The FTIR spectra were recorded on a Nicolet 6700 FTIR spectrometer (Thermo Scientific, Waltham, Massachusetts, USA), from 4000 to 400 cm^{-1} at room temperature. 128 scans were collected with a spectral resolution of 4 cm^{-1} in a nitrogen atmosphere. Background spectra (vacuum dried anhydrous MeOH on KBr) were recorded under identical conditions and subtracted.

3.5 Mass Spectrometry: Mass spectrometry analysis of the Zn-W complex solution was performed using an Acquity UPLC system, connected to a TQD XEVO triple quadrupole mass spectrometer with an electrospray ionization (ESI) source from Waters (Milford, MA, USA). The analysis was conducted in positive ionization mode.

3.6 Powder X-Ray Diffraction (PXRD) Analysis: The normalized XRD patterns were obtained in symmetrical Bragg geometry with Cu Kα radiation on Scintag (USA) powder diffractometer equipped with liquid nitrogen-cooled Ge solid-state detector.

4. Evaluation of Antibacterial Activity

Bacillus subtilis (B. subtilis), *Escherichia coli (E. coli)* and *Staphylococcus aureus (S. aureus)* two types of bacteria, were used to test Zn-W's antibacterial activity. GFP-tagged *E. coli* was a generous gift from Prof. Bama Charan Mondal, BHU, Varanasi, and *B. subtilis* was a generous gift from Prof. Avnish Parmar, IIT (BHU), Varanasi. *S. aureus* was obtained from Institute of Medical sciences, University in Varanasi, Uttar Pradesh

4.1 The Inhibition of Bacterial Growth

First, Luria Bertani (LB) medium was used to cultivate *E. coli*, S. aureus and *B. subtilis* cultures, which were then overnight incubated at 37°C to evaluate the effect of Zn-W on bacterial growth and proliferation. The culture of bacteria was mixed with fresh LB media the next day, and it was left to incubate until it reaches an optical density (OD) of 0.6. Then, 2 ml of LB medium were added in 24 well plate and combined with amoxicillin as positive control with a concentration of 1000 µg/ml, and different concentrations of Zn-W (500 µg/ml, 100 µg/ml, 50 µg/ml). After inoculating each medium with 20 µl of cultivated bacteria (*E.coli*) of (OD=0.6), growth kinetics were measured using a Synergy H1-Microplate reader in a time-dependent manner (0h, 2h, 4h, 6h, and 8h) at 600 nm.[29]

4.2 Study of the Bacterial Zone of Inhibition

Agar plates were aseptically plated with newly cultured 200 µl *E. coli*, *S.aureus* and *B. subtilis* at an optical density (OD) of 0.6 in order to assess Zn-W's antibacterial activity against these

two bacteria.[30] The Zn-W was then carefully soaked in Whatman filter paper discs at varied concentrations (100 µg/ml, 50 µg/ml, 10 µg/ml, and 1 µg/ml) and placed on agar plates to dry. The outcomes were compared with the group under positive control (1000 µg/ml). At 37°C, the plates were incubated for a full day. By measuring the zones that developed around the discs, the sample's antibacterial efficacy was evaluated.

4.3 Scanning Electron Microscope

Coverslips were first coated with Zn-W and incubated with bacteria (*E. coli*) for 24 hours, supplemented with 2 ml LB medium, to explore the antimicrobial properties of Zn-W. Following the incubation period, the coverslips were cleaned with phosphate buffer solution (PBS) and the bacterium adhered to the cover slips were fixed with 200 µl of 2.5% glutaraldehyde and 2% osmium tetroxide. The samples were dehydrated using a succession of increasing ethanol concentrations to and imaged using FEI Quanta 450 scanning electron microscope.[31]

4.4 Assessment of Intracellular Reactive Oxygen Species Production Production

A fluorescent-based 7′-dichlorodihydrofluorescein diacetate (DCFDA) assay was utilized to understand how intracellular Zn-W produces reactive oxygen species (ROS).[32] The conversion of 7′-dichlorodihydrofluorescein diacetate (DCFDA) to green fluorescent Dichlorofluorescein (DCF) was observed as the result of intracellular ROS. When ROS oxidise DCF, a green fluorescence is produced. Zn-W (500 µg/ml, 100 µg/ml, 50 µg/ml, and 10 µg/ml) were incubated with 200 µl of bacteria for the 8 h in the 2 ml of LB broth. After 8h, 150 µl of bacterial suspension with Zn-W were incubated with 50 µl of 10 (mM) of DCFDA in 96 black plates for 30 minutes at room temperature. The green fluorescence intensity was measured after five minutes (λex: 485 nm; λem: 528 nm)

4.5 Impact of Zn-W in the bacterium's extracellular polymeric substances

To examine Zn-W's antibacterial effects, we examined its effects on the extracellular polymeric substances (EPS) of bacteria.[33] 20 µL of an *E. coli* inoculum (at OD=0.6) was incubated with 2 mL of LB broth in a 12-well plate. Zn-W was introduced into each well at different quantities (50 µg/ml and 100 µg/ml). Untreated bacteria were kept as the control and amoxicillin (1000 µg/ml) as the positive control. For an entire day, the samples were maintained in a shaking incubator at 37 °C. A day later, the bacterial culture was taken out of the supernatant followed by temperature controlled (at 4 °C) centrifugation for half an hour at 6000 rpm. In order to separate the EPS, the supernatant was mixed with two volumes of acetone and refrigerated at 4 °C for the entire night. Lastly, the mixture was centrifuged for thirty minutes at 4 °C (6000 rpm) to extract the EPS[34] and the pellet's weight was measured.

4.6 Confocal Microscopy

Zn-W was incubated with green fluorescent protein bacteria (GFP-*E. coli*) in LB media in different groups (100 µg/ml, and 500 µg/ml) for two days. Untreated GFP-*E. coli* was kept as control group. Following the incubation period, the LB medium was centrifuged at 14,000 rpm for 15 minutes and the pellet was washed with PBS multiple times. The pellets were then stained using 200 µl of 4',6-diamidino-2-phenylindole (*DAPI)* (15 µg/ml) and 20 µl of propidium iodide stain (*PI)* (70 µg/ml). To get rid of any unbound staining molecules, the pellet was again washed with PBS[35] and fixed onto a glass slide using 2.5% glutaraldehyde. Following fixation, a confocal microscope (Zeiss 510 Meta confocal microscopy equipment) was used to capture images of live and dead bacteria at 63 X.[29]

4.7 Chorioallantoic membrane (CAM) assay

The chorioallantoic membrane (CAM) assay was used to inspect the biocompatibility of Zn-W on the development of blood arteries in the chicken embryo. For this experiment, fertilized eggs were obtained from a hatchery located in Varanasi, Uttar Pradesh. The eggs were incubated at 37 °C for four days. The egg's outer shell was slightly opened on the fifth day to reveal the evolving blood vessels. Whatman filter paper discs were soaked with Zn-W (100 µg/ml and 50 µg/ml) for two minutes and then placed upon the developing chick embryo. For a maximum of six hours, the effects of Zn-W on blood vessel creation and development were observed using a Magnus MagZoom TZM6 Trinocular Stereo Zoom Microscope. Untreated eggs were used as a control. Additionally, blood artery integrity parameters like length, junctions, and size were measured using Angiotool and Image J software's.

4.8 Cell viability analysis using the MTT assay

To investigate the impact of Zn-W on the viability of the human embryonic kidney 293 cell line (HEK-293), the 3-(4,5-dimethylthiazol-2-yl)-2,5-diphenyl tetrazolium bromide (MTT) test was used. 96-well plates were seeded with 1×10^4 cells. Following a 24-hour incubation period, three distinct concentrations of Zn-W were introduced as treatments (100, 50, and 10 µg/ml) and incubated for another 24-hour period. After the medium was removed, 100 µl (0.5 mg/mL) of MTT suspension was added, and the combination was then brought to 37 °C and incubated for 4 hours in an incubator with 5% CO2. After carefully removing the MTT solution, 100 µl of DMSO : MeOH (1:1) was added to break down the formazan crystal. A multiplate reader was used to measure the mixture's absorbance at 570 nm. The following formula was then used to determine the cell viability (%):

% cell viability = $\left(\frac{As}{Ac}\right) \times 100$

As and Ac denotes absorbance of sample and control at 570 nm.

4.8.1 Cell proliferation assay

HEK- 293 (100,000/well) cells were cultured in 24-well plate with Zn-W coated slides, incubated with 5-ethynyl-2'-deoxyuridine (EdU,10μM) for 24 h. Manufacturer protocol was used for this study (Puregene EdU cell proliferation imaging Assay Kit, Green AF488, # PG-673A-CK). We have used this method to determine the rate of cell proliferation. Confocal immunofluorescence microscopy was used for imaging of the cells incubated with our sample and compared with control.[36]

4.9 Scratch-wound assay for cell migration

Human embryonic kidney 293 cell line (HEK-293) 100,000/cells were seeded in 24- well plate in complete media and incubated at 37 °C and 5% CO_2 for 24 h. The 24-well plate's lid served as a straight-edged guide. Guided by the cover, the cell surface was scraped in a straight line with the wounding tool. For wells that were scraped by the wounding tool, the motion was repeated. After adding treatment of Zn-W at various concentration images of the cell were recorded up till 24 hr and compared with control.[37] Percentage wound closure was calculated as follows:

% of wound closure = $\left(\frac{Wound\ area\ on\ day\ 0 - Wound\ area\ on\ day\ N}{Wound\ area\ on\ day\ 0}\right) \times 100$

where N = wound area on the corresponding day.

4.10 Measurement of cellular internalized ROS

In 24-well culture dishes, human embryonic cells (HEK-293; 100,000 cells per well) were cultivated for 24 hours in the cell culture incubator, at 37 °C. Three types of cells were used to treat the human cell lines: untreated cells, cells with varying concentrations of Zn-W. The concentrations of Zn-W used were 500 μg/ml, 100 μg/ml, and 50 μg/ml and 10 μg/ml. After four hours, each well received 10 μl of DCFDA (30 μM), which was then left for thirty to forty minutes. PBS was used to properly wash the incubated cells two or three times. After that, 100 μl of Radioimmunoprecipitation assay (RIPA) buffer was added to the cells to lyse them, and they were maintained for 10 minutes at 4°C. Centrifuging the scraped cells for 10 minutes at 4 °C at 14,000 rpm yielded cell lysates. The fluorescence of both treated and untreated cells

was measured using a multimode reader with an excitation at λex = 485 nm and an emission at λem = 528 nm.

4.10.1 DPPH assay for antioxidant activity

The technique most commonly employed to evaluate a sample's antioxidant capacity is the 2,2-diphenyl-1-picrylhydrazyl (DPPH) test.[38] When DPPH, a purple dye, comes into contact with antioxidants, it turns yellow. To dissolve 0.78 milligrams of DPPH, 10 mL of 99.5% ethanol was used and kept in the dark for two hours. 1 ml of different concentration of Zn-W (500, 100, 50 and 10 µg/ml) were mixed with freshly prepared DPPH solution. The samples were left in the dark and at room temperature for thirty minutes. Using a bio spectrophotometer, the absorbance was measured at 517 nm with DPPH solution serving as the control. The following formula was utilized to calculate the percentage of scavenging activity:

% of scavenging activity = $\left(\frac{Ac-As}{Ac}\right) \times 100$

where, AC and AS denote the absorbance of the control and sample at 517 nm.

5. *In vivo* Studies

In vivo wound healing studies were performed after institutional IAEC approval (Protocol Number: IIT(BHU)/IAEC/2023/068; Approval Date: February 9, 2023). Healthy Wistar rats (6–7 weeks old; 150–200 g) were procured from the CDRI-Lucknow and kept in accordance with biosafety regulations. After a seven-day initial acclimatization period to the animal house, the tests commenced.

5.1 Wound healing study

For the in vivo wound healing investigation, the rats (n = 4) were randomly assigned to three groups: a) the Untreated control group; b) the Positive control group (Silver Nitrate Gel 0.2% W/W); and c) the Zn-W treated group (20 µg of Zn-W per rat wound). Initially, the rats were administered a combination of xylazine (10 mg/kg) and ketamine (50 mg/kg) hydrochloride intraperitoneally (i.p.) to induce anaesthesia. After shaving and sterilizing the skin's surface with 70% alcohol and 10% betadine, biopsy punches with a 10 mm diameter were used to create wounds.[39] Zn-W were applied locally using cotton gauze at each time interval (0, 3, 5, 7,9 and 11 days). Optical images were taken and the wounds were measured over the course of 11 days in order to continuously assess the effectiveness of wound healing. On day eleven, all of the rats were sacrificed, and samples of the skin from the wound area were taken and fixed for histological examination. Percentage wound closure was calculated as follows:

$$\% \text{ of wound closure} = \left(\frac{Wound\ area\ on\ day\ 0 - Wound\ area\ on\ day\ N}{Wound\ area\ on\ day\ 0}\right) \times 100$$

where N = wound area on the corresponding day.

5.2 Histology:

Skin tissue samples were embedded at optimal cutting temperature (OCT) and sectioned using a cryo-microtome into 20 µm thick slices. Following rehydration with a graded ethanol series (100%, 95%, 90%, 80%, 70%, 50%, and 30%), the sections placed on a glass slide were cleaned with PBS. The application of haematoxylin and eosin stain was done in accordance with the standard protocol. The thickness of the epidermis was also measured for all the groups by Image J analysis.

5.3 Immunohistochemistry: Collagen deposition

The slides were soaked in a succession of escalating ethanol concentrations (100%, 95%, 90%, 80%, 70%, 50%, and 30%) to dehydrate them after being coloured with 0.5% aniline blue solution for five minutes for collagen deposition study. Afterwards, they were mounted and examined under an optical microscope.

5.4 Alpha Smooth Muscle Stain Immunohistochemistry

Tissue rehydration was performed using a graduated ethanol series (100%, 95%, 90%, 80%, 70%, 50%, 30%) in order to prepare these for alpha smooth muscle stain (*α-SMA*) immunohistochemistry. There was a PBS wash after this. To achieve antigen retrieval, tissue slices were treated for five minutes at boiling temperature in a citrate solution. Sections were blocked for an hour with 6% bovine serum albumin (BSA) and 0.3% Triton X-100 in PBS, and then they were permeabilized with 0.5% Triton X-100. Application of the primary Alpha-smooth Muscle actin monoclonal antibody- Thermofisher scientific (*α-SMA* 1 µg/ml) was made overnight at 4 °C.[40] This was followed by several PBS washes. Goat anti-Mouse IgG2a Cross-Adsorbed Secondary Antibody, Alexa Fluor™ 594 was added at a concentration of 0.5 µg/ml along with 2 drops of *DAPI* to the section slides (for nucleus staining) and left for 1 hour for 4 °C. Consequently, several washings were performed using 1X PBS. Finally, the immunostaining images were taken using Zeiss and Model no. LSM -780 microscope, and the image was processed using ImageJ software.

5.5 Statistical Analysis

To make sure they were reliable and accurate, the trials were run minimum three times. Each experiment's results were displayed as the average value plus standard error. Using the Origin

program, a one-way analysis of variance (ANOVA) was carried out to ascertain the statistical significance of the observed data.

3.6 References

(1) Alam, W.; Hasson, J.; Reed, M. Clinical Approach to Chronic Wound Management in Older Adults. *J. Am. Geriatr. Soc.* **2021**, *69* (8), 2327–2334. https://doi.org/10.1111/jgs.17177.

(2) Saxena, S.; Punjabi, K.; Ahamad, N.; Singh, S.; Bendale, P.; Banerjee, R. Nanotechnology Approaches for Rapid Detection and Theranostics of Antimicrobial Resistant Bacterial Infections. *ACS Biomater. Sci. Eng.* **2022**, *8* (6), 2232–2257. https://doi.org/10.1021/acsbiomaterials.1c01516.

(3) Zhao, W.; Jiang, L.; Pan, W.; Li, D.; Duan, M.; Zhou, Y.; Chen, L. V2CTx-Au Nanostructures for Rapid Surface-Enhanced Raman Scattering Detection of Bacteria and Synergistic Photothermal/Photodynamic Therapy. *ACS Appl. Nano Mater.* **2024**, *7* (12), 14673–14683. https://doi.org/10.1021/acsanm.4c02222.

(4) Maslova, E.; Eisaiankhongi, L.; Sjöberg, F.; McCarthy, R. R. Burns and Biofilms: Priority Pathogens and in Vivo Models. *npj Biofilms Microbiomes* **2021**, *7* (1), 73. https://doi.org/10.1038/s41522-021-00243-2.

(5) Xie, X.; Sun, T. C.; Xue, J.; Miao, Z.; Yan, X.; Fang, W. W.; Li, Q.; Tang, R.; Lu, Y.; Tang, L.; Zha, Z.; He, T. Ag Nanoparticles Cluster with PH-Triggered Reassembly in Targeting Antimicrobial Applications. *Adv. Funct. Mater.* **2020**, *30* (17), 1–10. https://doi.org/10.1002/adfm.202000511.

(6) Li, Y.; Miao, Y.; Yang, L.; Zhao, Y.; Wu, K.; Lu, Z.; Hu, Z.; Guo, J. Recent Advances in the Development and Antimicrobial Applications of Metal–Phenolic Networks. *Adv. Sci.* **2022**, *9* (27), 1–22. https://doi.org/10.1002/advs.202202684.

(7) Nethi, S. K.; Das, S.; Patra, C. R.; Mukherjee, S. Recent Advances in Inorganic Nanomaterials for Wound-Healing Applications. *Biomater. Sci.* **2019**, *7* (7), 2652–2674. https://doi.org/10.1039/c9bm00423h.

(8) Halarnekar, D.; Ayyanar, M.; Gangapriya, P.; Kalaskar, M.; Redasani, V.; Gurav, N.; Nadaf, S.; Saoji, S.; Rarokar, N.; Gurav, S. Eco Synthesized Chitosan/Zinc Oxide Nanocomposites as the next Generation of Nano-Delivery for Antibacterial, Antioxidant, Antidiabetic Potential, and Chronic Wound Repair. *Int. J. Biol. Macromol.* **2023**, *242* (P1), 124764. https://doi.org/10.1016/j.ijbiomac.2023.124764.

(9) Teng, R.; Yang, Y.; Zhang, Z.; Yang, K.; Sun, M.; Li, C.; Fan, Z.; Du, J. In Situ Enzyme-Induced Self-Assembly of Antimicrobial-Antioxidative Peptides to Promote Wound Healing. *Adv. Funct. Mater.* **2023**, *33* (23), 1–10. https://doi.org/10.1002/adfm.202214454.

(10) Feng, P.; Kong, Y.; Liu, M.; Peng, S.; Shuai, C. Dispersion Strategies for Low-Dimensional Nanomaterials and Their Application in Biopolymer Implants. *Mater. Today Nano* **2021**, *15*, 100127. https://doi.org/10.1016/j.mtnano.2021.100127.

(11) Das, I. J.; Bal, T. PH Factors in Chronic Wound and PH-Responsive Polysaccharide-Based Hydrogel Dressings. *Int. J. Biol. Macromol.* **2024**, *279* (P1), 135118. https://doi.org/10.1016/j.ijbiomac.2024.135118.

(12) Chen, S.; Tong, X.; Huo, Y.; Liu, S.; Yin, Y.; Tan, M. L.; Cai, K.; Ji, W. Piezoelectric Biomaterials Inspired by Nature for Applications in Biomedicine and Nanotechnology. *Adv. Mater.* **2024**, *36* (35). https://doi.org/10.1002/adma.202406192.

(13) Li, M.; Qiu, W.; Wang, Q.; Li, N.; Liu, L.; Wang, X.; Yu, J.; Li, X.; Li, F.; Wu, D. Nitric Oxide-Releasing Tryptophan-Based Poly(Ester Urea)s Electrospun Composite Nanofiber Mats with Antibacterial and Antibiofilm Activities for Infected Wound Healing. *ACS Appl. Mater. Interfaces* **2022**, *14* (14), 15911–15926. https://doi.org/10.1021/acsami.1c24131.

(14) Najjari, A.; Mehdinavaz Aghdam, R.; Ebrahimi, S. A. S.; Suresh, S. K.; Krishnan, S.; Shanthi, C.; Ramalingam, M. Smart Piezoelectric Biomaterials for Tissue Engineering and Regenerative Medicine: A Review. *Biomed. Tech.* **2022**, *67* (2), 71–88. https://doi.org/10.1515/bmt-2021-0265.

(15) Sinha, A. K.; Laursen, M. F.; Brinck, J. E.; Rybtke, M. L.; Hjørne, A. P.; Procházková, N.; Pedersen, M.; Roager, H. M.; Licht, T. R. Dietary Fibre Directs Microbial Tryptophan Metabolism via Metabolic Interactions in the Gut Microbiota. *Nat. Microbiol.* **2024**, *9* (8), 1964–1978. https://doi.org/10.1038/s41564-024-01737-3.

(16) Anurag Anand, A.; Amod, A.; Anwar, S.; Sahoo, A. K.; Sethi, G.; Samanta, S. K. A Comprehensive Guide on Screening and Selection of a Suitable AMP against Biofilm-Forming Bacteria. *Crit. Rev. Microbiol.* **2024**, *50* (5), 859–878. https://doi.org/10.1080/1040841X.2023.2293019.

(17) Makam, P.; Yamijala, S. S. R. K. C.; Tao, K.; Shimon, L. J. W.; Eisenberg, D. S.; Sawaya, M. R.; Wong, B. M.; Gazit, E. Non-Proteinaceous Hydrolase Comprised of a Phenylalanine Metallo-Supramolecular Amyloid-like Structure. *Nat. Catal.* **2019**, *2* (11), 977–985. https://doi.org/10.1038/s41929-019-0348-x.

(18) Barth, A. The Infrared Absorption of Amino Acid Side Chains. *Prog. Biophys. Mol. Biol.* **2000**, *74* (3–5), 141–173. https://doi.org/10.1016/S0079-6107(00)00021-3.

(19) Cui, Z.; Jiang, P.; Leng, Y.; Zhihao, L.; Feng, S.; Mei, X.; Chen, S.; Sheng, X. A "One-pot" Method for Synthesizing Zinc Tryptophan and Its Derivatives as Highly Efficient <scp>PVC</Scp> Thermal Stabilizer with Excellent Mechanical Properties. *J. Appl. Polym. Sci.* **2024**, *141* (21), 1–19. https://doi.org/10.1002/app.55394.

(20) Mukherjee, S.; Chowdhury, D.; Kotcherlakota, R.; Patra, S.; Vinothkumar, B.; Bhadra, M. P.; Sreedhar, B.; Patra, C. R. Potential Theranostics Application of Bio-Synthesized Silver Nanoparticles (4-in-1 System). *Theranostics* **2014**, *4* (3), 316–335. https://doi.org/10.7150/thno.7819.

(21) Peng, H.; Rossetto, D.; Mansy, S. S.; Jordan, M. C.; Roos, K. P.; Chen, I. A. Treatment of Wound Infections in a Mouse Model Using Zn2+-Releasing Phage Bound to Gold Nanorods. *ACS Nano* **2022**, *16* (3), 4756–4774. https://doi.org/10.1021/acsnano.2c00048.

(22) Wang, M.; Wang, C.; Chen, M.; Xi, Y.; Cheng, W.; Mao, C.; Xu, T.; Zhang, X.; Lin, C.; Gao, W.; Guo, Y.; Lei, B. Efficient Angiogenesis-Based Diabetic Wound Healing/Skin Reconstruction through Bioactive Antibacterial Adhesive Ultraviolet Shielding Nanodressing with Exosome Release. *ACS Nano* **2019**, *13* (9), 10279–10293. https://doi.org/10.1021/acsnano.9b03656.

(23) Seon, G. M.; Lee, M. H.; Koo, M. A.; Hong, S. H.; Park, Y. J.; Jeong, H. K.; Park, J. C. A Collagen-AS/EPLL Bilayered Artificial Substitute Regulates Anti-Inflammation and Infection for Initial Inflamed Wound Healing. *Biomater. Sci.* **2021**, *9* (20), 6865–6878. https://doi.org/10.1039/d1bm01071a.

(24) Huang, P.; Xu, J.; Xie, L.; Gao, G.; Chen, S.; Gong, Z.; Lao, X.; Shan, Z.; Shi, J.; Zhou, Z.; Chen, Z.; Cao, Y.; Wang, Y.; Chen, Z. Improving Hard Metal Implant and Soft Tissue Integration by Modulating the "Inflammatory-Fibrous Complex" Response. *Bioact. Mater.* **2023**, *20* (May 2022), 42–52. https://doi.org/10.1016/j.bioactmat.2022.05.013.

(25) Ponsen, A. C.; Proust, R.; Soave, S.; Mercier-Nomé, F.; Garcin, I.; Combettes, L.; Lataillade, J. J.; Uzan, G. A New Hemostatic Agent Composed of Zn2+-Enriched Ca2+ Alginate Activates Vascular Endothelial Cells in Vitro and Promotes Tissue Repair in Vivo. *Bioact. Mater.* **2022**, *18* (September 2021), 368–382. https://doi.org/10.1016/j.bioactmat.2022.01.049.

(26) Shrestha, S.; Shrestha, B. K.; Tettey-Engmann, F.; Auniq, R. B. Z.; Subedi, K.; Ghimire,

S.; Desai, S.; Bhattarai, N. Zein-Coated Zn Metal Particles-Incorporated Nanofibers: A Potent Fibrous Platform for Loading and Release of Zn Ions for Wound Healing Application. *ACS Appl. Mater. Interfaces* **2024**, *16* (37), 49197–49217. https://doi.org/10.1021/acsami.4c13458.

(27) Qian, Y.; Zheng, Y.; Jin, J.; Wu, X.; Xu, K.; Dai, M.; Niu, Q.; Zheng, H.; He, X.; Shen, J. Immunoregulation in Diabetic Wound Repair with a Photoenhanced Glycyrrhizic Acid Hydrogel Scaffold. *Adv. Mater.* **2022**, *34* (29), 1–15. https://doi.org/10.1002/adma.202200521.

(28) Yang, N.; Venezuela, J.; Almathami, S.; Dargusch, M. Zinc-Nutrient Element Based Alloys for Absorbable Wound Closure Devices Fabrication: Current Status, Challenges, and Future Prospects. *Biomaterials* **2022**, *280* (July 2021), 121301. https://doi.org/10.1016/j.biomaterials.2021.121301.

(29) Nayak, M.; Sonowal, L.; Pradhan, L.; Upadhyay, A.; Kamath, P.; Mukherjee, S. Multifunctional (4-in-1) Therapeutic Applications of Nickel Thiocyanate Nanoparticles Impregnated Cotton Gauze as Antibacterial, Antibiofilm, Antioxidant and Wound Healing Agent. *Chem. - An Asian J.* **2024**, *19* (21). https://doi.org/10.1002/asia.202400187.

(30) Pan, X.; Kong, D.; Wang, W.; Liu, W.; Ou-Yang, W.; Zhang, C.; Wang, Q.; Huang, P.; Zhang, C.; Li, Y. Synthetic Polymeric Antibacterial Hydrogel for Methicillin-Resistant Staphylococcus Aureus-Infected Wound Healing: Nanoantimicrobial Self-Assembly, Drug- And Cytokine-Free Strategy. *ACS Nano* **2020**, *14* (10), 12905–12917. https://doi.org/10.1021/acsnano.0c03855.

(31) Lencova, S.; Svarcova, V.; Stiborova, H.; Demnerova, K.; Jencova, V.; Hozdova, K.; Zdenkova, K. Bacterial Biofilms on Polyamide Nanofibers: Factors Influencing Biofilm Formation and Evaluation. *ACS Appl. Mater. Interfaces* **2021**, *13* (2), 2277–2288. https://doi.org/10.1021/acsami.0c19016.

(32) Tu, C.; Lu, H.; Zhou, T.; Zhang, W.; Deng, L.; Cao, W.; Yang, Z.; Wang, Z.; Wu, X.; Ding, J.; Xu, F.; Gao, C. Promoting the Healing of Infected Diabetic Wound by an Anti-Bacterial and Nano-Enzyme-Containing Hydrogel with Inflammation-Suppressing, ROS-Scavenging, Oxygen and Nitric Oxide-Generating Properties. *Biomaterials* **2022**, *286* (January), 121597. https://doi.org/10.1016/j.biomaterials.2022.121597.

(33) Li, B.; Mao, J.; Wu, J.; Mao, K.; Jia, Y.; Chen, F.; Liu, J. Nano–Bio Interactions: Biofilm-Targeted Antibacterial Nanomaterials. *Small* **2024**, *20* (7), 1–42. https://doi.org/10.1002/smll.202306135.

(34) Banerjee, A.; Chowdhury, P.; Bauri, K.; Saha, B.; De, P. Inhibition and Eradication of Bacterial Biofilm Using Polymeric Materials. *Biomater. Sci.* **2022**, *11* (1), 11–36. https://doi.org/10.1039/d2bm01276f.

(35) Wu, S.; Xu, J.; Zou, L.; Luo, S.; Yao, R.; Zheng, B.; Liang, G.; Wu, D.; Li, Y. Long-Lasting Renewable Antibacterial Porous Polymeric Coatings Enable Titanium Biomaterials to Prevent and Treat Peri-Implant Infection. *Nat. Commun.* **2021**, *12* (1), 1–14. https://doi.org/10.1038/s41467-021-23069-0.

(36) Zheng, W.; Shen, H.; Cheng, Y.; Liu, L.; Sun, J.; Chu, Z.; Wang, W.; Qian, H. Au Nanorods Activate Zn2+/Ag+ Mediated Anti-Inflammatory for Enhanced Methicillin-Resistant Wound Repair via Bionic Claw Microneedles. *ACS Mater. Lett.* **2024**, *6* (10), 4791–4800. https://doi.org/10.1021/acsmaterialslett.4c01546.

(37) Yang, J.; Chu, Z.; Jiang, Y.; Zheng, W.; Sun, J.; Xu, L.; Ma, Y.; Wang, W.; Shao, M.; Qian, H. Multifunctional Hyaluronic Acid Microneedle Patch Embedded by Cerium/Zinc-Based Composites for Accelerating Diabetes Wound Healing. *Adv. Healthc. Mater.* **2023**, *12* (24), 1–12. https://doi.org/10.1002/adhm.202300725.

(38) Liu, X.; Sun, Y.; Wang, J.; Kang, Y.; Wang, Z.; Cao, W.; Ye, J.; Gao, C. A Tough, Antibacterial and Antioxidant Hydrogel Dressing Accelerates Wound Healing and Suppresses Hypertrophic Scar Formation in Infected Wounds. *Bioact. Mater.* **2024**, *34* (December 2023), 269–281. https://doi.org/10.1016/j.bioactmat.2023.12.019.

(39) Zhou, L.; Dai, C.; Fan, L.; Jiang, Y.; Liu, C.; Zhou, Z.; Guan, P.; Tian, Y.; Xing, J.; Li, X.; Luo, Y.; Yu, P.; Ning, C.; Tan, G. Injectable Self-Healing Natural Biopolymer-Based Hydrogel Adhesive with Thermoresponsive Reversible Adhesion for Minimally Invasive Surgery. *Adv. Funct. Mater.* **2021**, *31* (14), 1–13. https://doi.org/10.1002/adfm.202007457.

(40) Li, R.; Liu, K.; Huang, X.; Li, D.; Ding, J.; Liu, B.; Chen, X. Bioactive Materials Promote Wound Healing through Modulation of Cell Behaviors. *Adv. Sci.* **2022**, *9* (10), 1–22. https://doi.org/10.1002/advs.202105152.